Escape Maps

Gustavo Machado, Filip Sadlo, *Member, IEEE*, Thomas Müller, and Thomas Ertl, *Member, IEEE*

Fig. 1. Escape maps at the example of coronal hole extraction. **(a)** Traditional visualization of coronal holes (yellow, light blue) by directly seeding field lines at the photosphere suffers from discretization problems. The visualization result suggests that (i), (ii), and (iii) might be connected by corridors, but it is impossible to resolve them with this approach. **(b)** Our escape map extraction obtains coronal hole boundaries (red, blue) by seeding field lines at boundary curves (orange) of trimmed isocline surfaces (green). **(c)** Isocline-based escape map extraction captures the full structure of coronal holes, revealing the corridor between (ii) and (iv).

Abstract—We present a technique to visualize the streamline-based mapping between the boundary of a simply-connected subregion of arbitrary 3D vector fields. While the streamlines are seeded on one part of the boundary, the remaining part serves as escape border. Hence, the seeding part of the boundary represents a map of streamline behavior, indicating if streamlines reach the escape border or not. Since the resulting maps typically exhibit a very fine and complex structure and are thus not amenable to direct sampling, our approach instead aims at topologically consistent extraction of their boundary. We show that isocline surfaces of the projected vector field provide a robust basis for streamsurface-based extraction of these boundaries. The utility of our technique is demonstrated in the context of transport processes using vector field data from different domains.

Index Terms—Streamline behavior, vector field topology, isocline surfaces, coronal hole extraction.

◆

1 INTRODUCTION

Vector fields are a concept at the core of science and engineering. Since they typically represent transport or a directional property in general, their analysis usually needs to take into account their global structure, which is reflected by integral curves such as streamlines. While there is a large body of literature on the visualization based on integral curves, there is a subfield, denoted vector field topology, which aims at the extraction of the global structure of streamlines. In analogy to geometric topology, one analyzes the connectivity of the domain by means of streamlines, i.e., regions that exhibit coherent streamline shape represent connected regions and are visualized as such. To do so, the boundaries between these regions are of particular interest—they represent so-called separatrices that separate the qualitatively different regions, and in unbounded domains, they represent manifolds of streamlines that converge in forward or reverse direction to critical points, which are isolated zeros of the vector field, or to periodic orbits, which are isolated closed streamlines. Hence, to decide if a quantity can be transported by a vector field between two points, it

is sufficient to test if these two points reside in the same region of coherent behavior. An impeding difficulty with this approach, however, arises if the domain is bounded or if the transport in subregions is of interest. In such cases, concepts from traditional vector field topology cannot provide the answer in generic configurations because the required critical points, periodic orbits, and separatrices can be located (partially) outside the domain and are hence not available.

Our approach is intrinsically independent of constructs such as critical points or periodic orbits. It can determine streamline-based connectivity between the boundary of arbitrary simply-connected regions Ω of the domain, and hence extends traditional vector field topology. To this end, one simply-connected part of the boundary of Ω is defined as *map boundary* where streamlines are conceptually seeded, and the remaining part of the boundary is the *escape boundary*. Our technique then provides a map, which we call *escape map*, on the map boundary, indicating if a streamline seeded at the respective position reaches the escape boundary or not. Thus, escape maps do not map to the position of escape but they provide a map *if* a respective streamline escapes. We refer to those parts of the map that escape as *escape regions* and to those that do not escape as *rest regions*. The boundaries between escape regions and rest regions are denoted *escape region boundaries*. Applications of escape maps include cases where one is interested if a substance can leave a region under the transport of a flow, for example, in the context of pollution or supply.

A straightforward implementation to obtain the streamline-based mapping between the map boundary and the escape boundary would

---

- *Gustavo Machado, Filip Sadlo, Thomas Müller, and Thomas Ertl are with University of Stuttgart, Germany.*
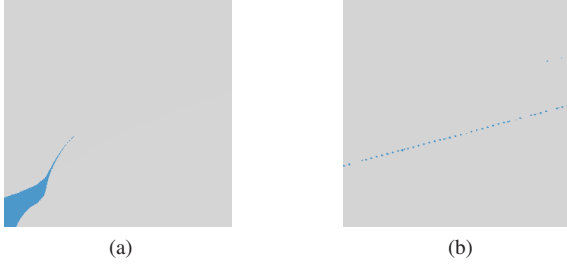 *E-mail: {machadgo,sadlo,muelleta,ertl}@visus.uni-stuttgart.de.*

Fig. 2. (a) Closeup of Fig. 1(a) at right-upper tip of coronal hole (ii), at zoom factor 16. It is impossible to judge whether there is a corridor between (ii) and (iv). (b) View at the center of (a) at zoom factor 5,000. The corridor appears here because its width is wider in vicinity to (ii). However, numerical precision issues are apparent, prohibiting further zooming and hence identification of the corridor farther away from (ii).

Fig. 3. Parametrization $\mathbf{x}(\xi, \eta, \zeta)$ of the simulation domain Ω with illustrated streamlines (black) and corresponding isocline surface (green). (a) Arbitrary simply-connected region in physical space with map boundary $\partial\Omega_M$ (red) and escape boundary $\partial\Omega_E$ (dashed). The dotted lines can serve either as escape or as periodic boundaries. (b) Computational space represented by the parameters (ξ, η, ζ).

be to densely seed streamlines on the map boundary, test if they reach the escape boundary in forward or reverse direction of integration, and label the seed points accordingly. This approach has been already used in the astrophysics community to analyze *coronal holes*, which represent regions of the Sun's photosphere with reduced ultraviolet or X-ray emission, and are defined in this context as those regions on the photosphere that exhibit streamlines of the solar magnetic field that reach, in forward or reverse direction, an escape radius which is larger than the radius of the photosphere. In this configuration, the photosphere represents the map boundary, and the escape radius defines the escape boundary. The extraction of coronal holes is one of the applications that we demonstrate our approach with, among examples from computational fluid dynamics and magma convection in the Earth's mantle.

The major difficulty with this direct sampling approach (Fig. 1(a)) is, however, that it is typically not able to reveal the correct structure of the escape map because this map typically exhibits extremely thin features which cannot be appropriately sampled with a regular sampling (Figs. 1 and 2). At the same time, these fine structures typically exhibit diverging streamlines, which leads to strong error accumulation during integration from the map boundary and hence inaccurate or even useless streamlines and resulting mappings.

In this work, we show, to the best of our knowledge for the first time, the close connection between the topological concept of escape maps and isocline surfaces of the vector field, and derive from this connection a sampling technique for escape maps that guarantees their topologically correct extraction. Since our approach extracts only escape region boundaries, i.e., the boundary curves between escape regions and rest regions of the escape map (Fig. 1(c)), we complement our technique with a view-dependent implementation of the straightforward sampling approach, demonstrated in Fig. 1(a).

Specifically, our contributions include:

- The introduction of escape maps to scientific visualization,

- a topologically correct and robust extraction technique for the escape region boundaries within escape maps,

- derivation of the connection between isocline surfaces and concepts from vector field topology, and

- a view-dependent implementation for direct sampling-based visualization of escape maps.

2 RELATED WORK

Since both the concept and our extraction technique for escape maps are closely related to vector field topology, we start with an overview on related work in this field. Vector field topology was introduced to scientific visualization by the works due to Perry and Chong [22], Helman and Hesselink [9, 10], and Globus et al. [8]. At the core of this concept is the search for invariant manifolds, i.e., streamlines that are
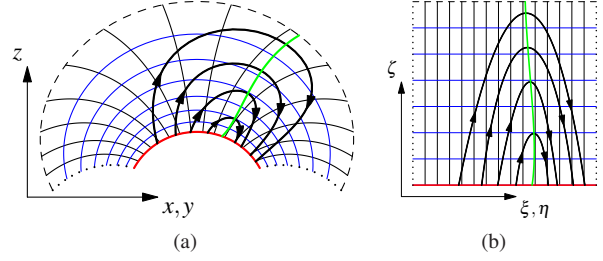
invariant under variation of integration length. One example are periodic orbits, which Wischgoll et al. [30] and Kasten et al. [13] present extraction techniques for. We refer the reader to Asimov's notes on topology [4] for an introduction. More recently, vector field topology has been extended to uncertain [19, 20] and time-dependent [28] vector fields. Other conceptual contributions to this field include saddle connectors [25] and connectrices [5]. Scheuermann et al. [24] include the domain boundary in topological analysis to avoid missed topological structures in 2D vector fields. Other related work includes traditional topological visualization in constrained flow fields [21]. However, to determine regions of qualitatively similar behavior, all these techniques, in contrast to ours, require that the respective constructs, i.e., critical points or periodic orbits, reside within the domain.

There are two previous works that are closely related to our technique. The boundary switch connectors due to Weinkauf et al. [29] introduce boundary switch curves, i.e., curves on the boundary of Ω at which the 3D vector field switches from inside to outside flow behavior, and separation surfaces consisting of streamsurfaces seeded at these curves. This technique is also independent of critical points and periodic orbits, and provides a topological analysis on bounded domains. However, as we will show below, it is in general not possible to obtain escape maps with this approach, also because boundary switch curves are constrained to the boundary of Ω. Nevertheless, there are cases where part of the escape region boundaries in our escape maps can be obtained using boundary switch curves. The second technique that is closely related are bifurcation lines and their manifolds [15]. Bifurcation lines can be seen as a generalization ('elongation') of saddle-type critical points, i.e., they represent streamlines that locally over the longest time exhibit a 2D manifold of streamlines converging to them in forward time and a 2D manifold of streamlines converging to them in reverse time. Bifurcation lines also address topological analysis in bounded domains, they are able to extract 2D manifolds of saddle-type critical points that reside outside Ω or saddle periodic orbits, including their 2D manifolds, even if part of the orbit is located outside Ω. It has to be noted that both techniques ([29] and [15]) are somewhat complementary, i.e., boundary switch curves in general cannot extract the manifolds that bifurcation lines do and vice versa. Nevertheless, as we will also show below, bifurcation lines (and their manifolds) in general cannot extract escape maps either.

In the related application domain of solar magnetic fields, escape map extraction corresponds to the determination of coronal holes. Due to the lack of sensing techniques that would be able to provide 3D data of the Sun's magnetic field, there are different approaches that extrapolate such data from line of sight magnetograms. The most realistic approach makes use of a full 3D global magnetohydrodynamics (MHD) model (Mackay and Yeates [18]). Precomputed datasets with magnetic fields (MAS) given in spherical coordinates can be downloaded from the *Predictive Science Modeling Support for Helioseismic and Magnetic Imager Solar Dynamics Observatory* [2]. A review of coronal holes and a historical overview is given by Cranmer [7]. A quite recent technique for automatic detection of coronal holes based on im-
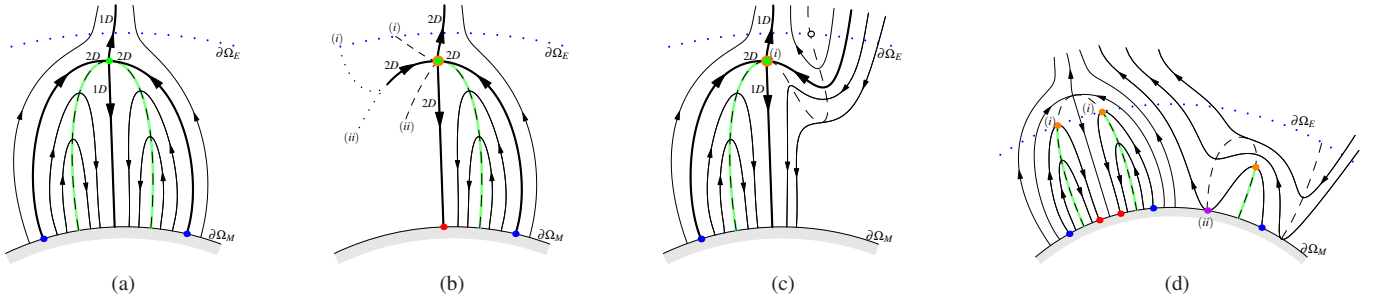
Fig. 4. Cross-sectional illustration of different 3D cases. If topological features (e.g., saddle points or saddle orbits, green dots) reside within Ω, then escape region boundaries (red, blue) are obtained by intersecting 2D manifolds of saddle-type critical points (a) or periodic orbits (b) with the map boundary $\partial\Omega_M$ (light gray). (d) Otherwise, escape region boundaries are obtained by intersecting $\partial\Omega_M$ with streamlines starting at boundaries (orange) of trimmed isocline surfaces (green curves). If this boundary resides at $\partial\Omega_M$ (purple point (ii) in (d)) there may be only one streamline connecting from (ii) to $\partial\Omega_E$. This boundary (purple) also represents a part of the escape region boundary and an inbound boundary switch curve. (c) If a critical point resides within Ω but part of its 2D manifold reaches the escape boundary $\partial\Omega_E$, there is also an isocline surface reaching $\partial\Omega_E$ and the 'top' (orange) of its trimmed part generates the escape region boundary.

age segmentation is described by Kristan and Galagher [14]. Riley et al. [23] use simple field line integration starting from the photosphere to detect coronal holes. Machado et al. [17], propose volume rendering-based techniques for visualizing the solar magnetic field. Cai et al. [6] applied traditional vector field topology to the Earth's magnetotail. However, in contrast to our approach, none of these techniques can guarantee topologically correct extraction of coronal holes.

3 EXTRACTION OF ESCAPE REGION BOUNDARIES

Let us start with an introduction of the different terms and symbols. The *map boundary* and *escape boundary* are denoted $\partial\Omega_M$ and $\partial\Omega_E$, respectively. Both have to be simply connected and together they enclose a simply-connected region Ω. If a streamline seeded on $\partial\Omega_M$ reaches $\partial\Omega_E$ in forward or in reverse direction, we refer to it as *escape streamline*, otherwise as *rest streamline*.

As a prerequisite for the formulation that will follow, we first need to provide Ω with a regular parametrization $\mathbf{x}(\xi,\eta,\zeta)$. (Here and in the following, we use boldface symbols to indicate vector-valued functions.) In this parametrization, the map boundary $\partial\Omega_M$ is represented by the set $\{\mathbf{x}(\xi,\eta,0)\}$ and the escape boundary $\partial\Omega_E$ is composed of the subsets $\partial\Omega_t = \{\mathbf{x}(\xi,\eta,1)\}$ and $\partial\Omega_s = \{\mathbf{x}(\pm 1, \pm 1, \zeta)\}$ if Ω is not periodic in ξ and η. Thus, $\mathbf{x}(\xi,\eta,\zeta)$ maps the computational space coordinates ξ, η, ζ to the physical space Cartesian coordinates x, y, z, see Fig. 3.

Given Ω is a rectangular domain, determining a regular parametrization $\mathbf{x}(\xi,\eta,\zeta)$ is straightforward. If Ω has generic simply-connected shape, however, the problem is equivalent to meshing Ω with a structured grid. Following Thompson [26], this could be accomplished by solving a boundary-value problem of the Laplacian equation, for example.

Our technique extracts escape region boundaries, i.e., the curves on $\partial\Omega_M$ that separate escape regions from rest regions. In the first step of our technique, the escape region boundary curves are extracted based on isocline surfaces of the vector field (Sec. 3.2). This step typically extracts the majority of the boundary curves. The remaining curves are extracted based on vector field topology features within Ω (Sec. 3.3). Algorithmic (discretization) details are given in Sec. 4.

3.1 Motivation

The straightforward approach to visualize escape maps is by *direct sampling*. This approach consists of seeding a set of streamlines on $\partial\Omega_M$ and color their starting point with one of three different colors: (i) (in our examples blue) indicating that the streamline reaches $\partial\Omega_E$ in forward direction, (ii) (yellow) indicating that the streamline reaches $\partial\Omega_E$ in reverse direction, and (iii) (gray) indicating that the streamline does not reach $\partial\Omega_E$. Note that if the streamline reaches $\partial\Omega_E$ in both directions, it represents an inbound boundary switch curve [29]. However, since such curves do not separate escape regions

from rest regions (in fact they separate forward escape regions from reverse escape regions), they are of no particular interest. Nevertheless, our extraction technique obtains them. The straightforward sampling approach is traditionally applied in a static manner, i.e., a texture is built with these colors and mapped to the physical space. Unfortunately, this approach cannot extract very narrow escape regions (corridors), as illustrated by Figs. 1(a) and 2. Note that, in favor of the direct sampling approach, we compare our technique to a view-dependent implementation of the direct sampling, i.e., the figures in this paper show a 'texture' that is computed interactively at screen resolution. This allows the user to zoom at the desired features interactively. There are two major reasons why the straightforward approach still fails at resolving the corridors: the corridors are extremely narrow and hence extremely high zoom factors would be required, which would lead to numerical issues with sampling, and secondly, streamline integration is subject to numerical issues too (Fig. 2), even with double-precision arithmetic. This is of particular impact in these configurations as the growth of integration error is much higher in the direction from corridors on $\partial\Omega_M$ compared to integration toward corridors on $\partial\Omega_M$, because streamlines have to diverge in direction away from $\partial\Omega_M$ to cause a narrow escape region, and this diverging streamline behavior represents unpredictable advection and hence typically impedes proper integration. Therefore, it is very difficult to discretize the fine structures on $\partial\Omega_M$ in a pixel-based manner. In contrast, it turns out to be much simpler to generate seeding constructs at some distance from $\partial\Omega_M$ and to obtain therefrom a polyline representation of the escape region boundaries, because streamlines converge toward the corridors in this direction of integration and thus are typically highly accurate.

3.2 Isocline Surface-Based Extraction Step

Escape maps are defined by the topological connectivity between $\partial\Omega_M$ and $\partial\Omega_E$. Since topological properties are invariant under continuous deformation, the connectivity between $\partial\Omega_M$ and $\partial\Omega_E$ is equivalent in both physical and computational space. Hence, our extraction technique can operate in computational space. Unless stated explicitly, we refer to the velocity field in computational space as 'vector field' throughout this paper. In the following, we discuss the utility of isocline surfaces (Sec. 3.2.1), subsequently, we present the extraction technique (Sec. 3.2.2), followed by its discussion (Sec. 3.2.3).

3.2.1 Motivation

Isocline surfaces consist of the loci where a vector field exhibits a predefined slope. Zero-slope isocline surfaces can be obtained by computing the dot product between the vector field and the 'up' vector (in our case $(0,0,1)^\top$ in computational space) and extracting the zero-level isosurface from the resulting scalar field, denoted *isocline surface* or *isocline* henceforth. See the dashed/green curves in Figs. 3 and 4 for illustrations of zero-slope isoclines.

Since our rest streamlines, i.e., those that do not escape, are continuously differentiable and bounded by $\partial\Omega$, they must (i) converge to a critical point, (ii) find some kind of infinite path inside Ω, e.g., toward a periodic orbit, or (iii) rise from $\partial\Omega_M$ and return to $\partial\Omega_M$ again. Since critical points are zeros of the vector field, they must reside on isocline surfaces. The case (ii) of an infinite path in a bounded region implies a return of the streamline, and, thus, in the non-degenerate case, a zero slope in at least two and at most an even number of points along the curve. The case (iii) must, due to the mean value theorem, exhibit an odd number of zero-slope points along the streamline. Hence, all cases exhibit at least one intersection with the isocline surface. Therefore, any rest streamline seeded on $\partial\Omega_M$ will intersect the isocline surface at least once. If we reject all parts of isocline surfaces that are intersected by an escape streamline, we obtain a *trimmed isocline surface* Θ, and its boundary curves $\partial\Theta$ are necessary and sufficient seeding structures to obtain all rest streamlines that connect to an escape region boundary. Once we propagate $\partial\Theta$ along the vector field both in forward and reverse direction, their intersection with $\partial\Omega_M$ will be at an escape region boundary. Note that boundary curves $\partial\Theta$ that are directly located on $\partial\Omega_M$ are either between escape and rest regions or between forward and backward escape regions (and in both cases inbound boundary switch curves).

3.2.2 Technique

1. Extract all isocline surfaces with slope zero relative to $\partial\Omega_M$, i.e., extract the zero-level isosurface of the 'up' component of the vector field within Ω. Note that the isosurfaces are closed or exhibit a boundary at $\partial\Omega_E$ and/or $\partial\Omega_M$.

2. Erode all parts of these surfaces that exhibit escape streamlines.

3. For each remaining surface part, extract its boundary curve.

4. Use these boundary curves as seeds for streamsurfaces.

5. The intersection curves of all streamsurfaces with $\partial\Omega_M$ represent escape region boundary parts.

Figure 1(c) shows the final result after merging the (partial) escape region boundaries obtained in this step with the results from the topology-based step (Sec. 3.3).

3.2.3 Discussion

The approach described in Sec. 3.2.2 cannot produce false positives in a continuous formulation. The cases depicted in Figs. 4(a)–(c) are simplified (degenerate)—in general, a critical point, periodic orbit, or bifurcation line would never be located exactly at the 'highest' point of an isocline surface with its 2D manifold aligned with the isocline. Thus, in general, at least a small part of the isocline surface is located above the 2D manifold and hence eroded, leaving a 'hole'. Integrating a streamsurface from the boundary of this hole in forward direction converges to the critical point, periodic orbit, or bifurcation line, since in the continuous case, this boundary coincides with the 2D manifold. However, in a discretized formulation (our implementation), the isocline surface is eroded a bit too much due to discretization and hence the stream surface is likely to miss the critical point, periodic orbit, or bifurcation line. It will rather deviate to the bottom and intersect $\partial\Omega_M$ at the red point in Fig. 4(b), leading to a false positive. The reverse streamsurface, on the other hand, will successfully extract the blue points in Figs. 4(a)–(c). Therefore, in our implementation, we avoid false positives by integrating streamsurfaces seeded at isocline boundaries only in direction opposite to the streamlines that caused the erosion of that isocline boundary (no streamsurface is seeded in case of forward and reverse escape). To assure robust extraction of the escape region boundaries, we nevertheless apply the topology-based approach (Sec. 3.3) also in our discretized implementation.
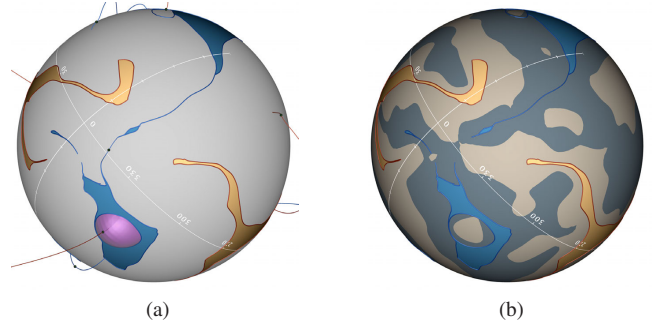

(a)   (b)

Fig. 5. MAS data at Carrington rotation 2128. **(a)** Same as Fig. 1, but with critical points (green) and their 1D (blue stable, red unstable) and 2D (transparent pink) manifolds. It is apparent that the topology-based step provides only very few boundaries (i.e., the intersection of the 2D manifold with the photosphere $\partial\Omega_M$) of the coronal holes. **(b)** Same as Fig. 1(c) but with polarity of the photosphere, i.e., radial magnetic flux B_r at photosphere, visualized. One can see that the three blue coronal holes belong to the same connected component of 'north' polarity.

3.3 Topology-Based Extraction Step

Because escape regions give rise to streamlines that reach $\partial\Omega_E$, in contrast to those seeded at rest regions, these two regions exhibit qualitatively different streamline behavior. Hence, extraction by concepts from vector field topology is an obvious choice. One such concept are separatrices, i.e., manifolds of streamlines converging in forward or reverse direction to saddle-type critical points or saddle-type periodic orbits. They represent barriers with respect to qualitatively different streamline behavior and should therefore be able to provide the boundaries of escape regions. Note that a saddle-type critical point, i.e., an isolated zero of the vector field with opposite signs of the real eigenvalue parts of the Jacobian, exhibits one 2D manifold and one 1D manifold, while a saddle-type periodic orbit, i.e., an isolated closed streamline with saddle-type behavior in its mapping under a full revolution, exhibits two 2D manifolds. Note that in this paper we refer to n-twisted-saddle periodic orbits as saddle-type periodic orbits.

In an unconstrained setup ($\partial\Omega_E \to \infty$), one could define escape streamlines as those that reach infinity. Escape region boundaries could then be obtained by intersecting the 2D separatrices of saddle points and saddle orbits with $\partial\Omega_M$ (cross-section illustration in Figs. 4(a) and 4(b)), with the additional requirement that, in case of a saddle, one end of its 1D manifold connects to $\partial\Omega_M$ and the other reaches $\partial\Omega_E$, and that in case of a saddle-type periodic orbit, both 2D manifolds connect to $\partial\Omega_M$ while at least one of its 2D manifolds reaches $\partial\Omega_E$. This approach, to some extent, is also possible in constrained setups (with non-empty $\partial\Omega_E$) as long as the required critical points and periodic orbits reside within Ω. Hence, we make use of this approach for all saddle-type critical points within Ω. However, as discussed above, this approach alone (without the isocline-based approach) would be insufficient even in the unconstrained setup because boundary switch curves (Fig. 4(d) (ii)) can also give rise to non-escape streamlines in absence of a saddle-type critical point, and bifurcation lines too. Furthermore, if a 2D manifold intersects $\partial\Omega_M$ only in one area but reaches $\partial\Omega_E$ in an other area, as illustrated in Fig. 4(c), there is always an isocline surface also reaching $\partial\Omega_E$ and hence the respective escape region boundary (part) is already extracted in Sec. 3.2.2.

3.3.1 Technique

1. Extract all saddle-type critical points within Ω.

2. For each saddle, one end of its 1D manifold has to connect to $\partial\Omega_M$ and the other has to connect to $\partial\Omega_E$ (Fig. 4(a)), otherwise the saddle is rejected.

3. Finally, intersect all 2D manifolds of the remaining saddles with $\partial\Omega_M$. The resulting intersection curves represent the missing escape region boundary parts.

(a)   (b)   (c)
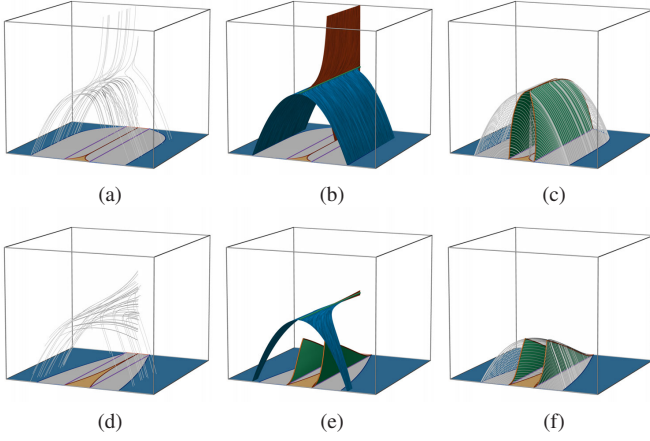
(d)   (e)   (f)

Fig. 6. Analytic field, Eq. (1), with $\lambda = 2$ ((a)–(c)) and $\lambda = 10$ ((d)–(f)). (a) Some streamlines together with escape map from our approach. Boundary switch curves [29] (violet) are all outbound and not consistent with escape map, hence not able to extract escape map. (b) Bifurcation line [15] (green) exhibits stable (blue) and unstable (red) manifold, which intersect map boundary at escape region boundaries. However, they provide only small straight parts. (c) Our eroded isocline surface (green) with streamsurfaces (illustrated by selected streamlines) seeded at its boundary provides the complete map. (d)–(f) Corresponding case for $\lambda = 10$. Note that bifurcation manifolds fail here too (also because isoclines do not reach bifurcation line) but our approach succeeds.

Figures 5(a) and 10(b) give an example of the (partial) escape region boundaries obtained in this step.

3.3.2 Discussion

We discussed in Sec. 3.2.3 that our isocline-based approach may miss 2D manifolds of critical points due to discretization issues and therefore we extract them explicitly in Sec. 3.3.1. The main difficulty with isocline-based extraction of 2D manifolds of saddle-type critical points is that the critical points are always located on the isocline surfaces and that, due to discretization issues, the erosion may fail to erode those parts of the isocline surfaces that contain the critical points. The circumstances are, however, different for saddle-type periodic orbits. A non-degenerate (i.e., not perfectly 'horizontal') periodic orbit intersects isocline surfaces only at isolated points. Hence, for reasons analogous to those discussed above with Fig. 4(c), saddle-type periodic orbits are robustly extracted already with our isocline-based approach (see also our bifurcation line-based evaluation in Sec. 3.4).

3.4 Evaluation

We first would like to provide a short comparison to previous work, i.e., to boundary switch curves and their separation surfaces [29] on the one hand, and bifurcation lines and their manifolds [15] on the other hand. We base the comparison on the following vector field:

$$\mathbf{u}(\mathbf{x}) := \left(-x, 4 - (0.4x)^2 - (0.1y)^2, \lambda\right)^\top. \quad (1)$$

As illustrated in Fig. 6, this field does neither contain a critical point nor a periodic orbit, but it exhibits a bifurcation line (green line) in z-direction. Its stable manifold (blue) intersects the y-max plane with its both sides, and in the case where $\lambda = 2$ the unstable manifold (red) intersects both the y-min and y-max plane of the shown region $[-30, 30] \times [-45, 5] \times [-30, 30]$. For our tests, we discretized the region on a Cartesian grid with resolution of $60 \times 50 \times 60$ nodes.

It can be seen that the escape map (which is located at $y = 5$) of this field exhibits a corridor, and that neither the outbound boundary switch curves (and their separation surfaces) nor bifurcation manifolds can extract the escape map here, and hence in general configurations.
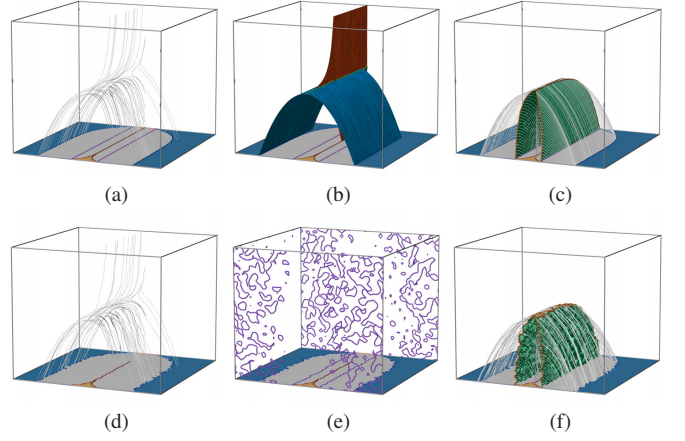

(a)   (b)   (c)

(d)   (e)   (f)

Fig. 7. Same as Figs. 6(a)–(c) but after applying 2% (upper row) and 30% of white noise (bottom row). The extracted bifurcation line is already disrupted at 2% (b), while our approach (c) still extracts the complete corridor. In case of 30% noise, we were not able to extract the bifurcation line (e), which can indicate the structural stability of the bifurcation line. In this case, our technique extracts only a spike, but still without disruptions, and consistent with streamline behavior (f).

To the best of our knowledge, our isocline-based approach is the only technique that robustly extracts escape maps.

We conclude our evaluation by examining the structural stability of escape maps, i.e., their robustness against perturbations. At the same time this gives a notion on the numerical stability of our extraction approach. To this end, we add different levels of white noise to Eq. (1) with $\lambda = 2$ (Fig. 7). While again, the boundary switch curve approach fails in both cases, the bifurcation manifold approach is not substantially affected with 2% noise. However, with 30% noise, we were not able to extract a bifurcation line or its manifolds. Still, our technique extracts an escape map without disruptions or other artifacts and the streamlines are consistent. Nevertheless, such an analysis can only give an impression of the structural stability versus numerical stability. Deriving the structural stability of bifurcation lines and relating them to integration error would exceed the scope of this paper. Taking into account persistence could be also a promising direction of research.

4 IMPLEMENTATION DETAILS

The description of our technique was, up to now, mostly in terms of continuous concepts. Here, we provide implementation details, in particular regarding discretization. Our entire implementation works in double precision, including the parts on the GPU.

4.1 Parameters

While the approach of direct sampling-based escape map extraction provides one conceptual parameter, the escape boundary $\partial \Omega_E$, the implementation of our approach requires a few additional parameters. The primary parameter is the discretization size of the resulting escape region boundaries. It is controlled by the maximum length δ of the segments of the resulting polyline representation. This parameter is used for inserting new trajectories during streamsurface computation (Sec. 4.4). Further parameters are the step size for line integration, the cell and mesh subdivision levels for isocline extraction, the maximum number of bisection steps for trimming (erosion), and the number of subdivision steps for the extraction of critical points.

4.2 Data Representation

Because our prototype operates almost entirely on the GPU and to ensure maximum performance, it supports in its present state any type of structured grid, i.e., any curvilinear grid. Nevertheless, extending the implementation for data on unstructured grids is straightforward.

The Buoyant Flow example covered in Sec. 5.1 is given on a uniform grid, while the Solar MHD data presented in Sec. 5.2 are given on spherical curvilinear grids, and the Magma Flow dataset, covered in Sec. 5.3, is also given on a spherical curvilinear grid.

4.3 Line Integration

Streamline integration is an essential step in our overall approach. It is required to obtain the 1D and 2D manifolds in the vector field topology step, as well as to trim the isocline surfaces, and to compute streamsurfaces therefrom. Hence, a fast implementation is required, which we realized on the GPU using the standard fourth-order Runge-Kutta scheme. The scheme is applied in computational space to exploit the topology of the structured grid and, more important, to ease the implementation and to improve the efficiency on the GPU.

4.4 Streamsurface Integration

Although we provide triangulated streamsurfaces for illustration purposes of the 2D manifolds, our approach does not require an explicit surface representation. The ordered set of streamlines is sufficient to obtain the intersection curves between the streamsurfaces and $\partial \Omega_M$. This allows us to follow the rather simple approach due to Hultquist [11], but it also allows us to omit the triangle generation step, similar to Machado et al. [16]. Hence, it is sufficient to start field lines at the seeding curve and to detect if neighboring lines diverge too far from each other, i.e., if their distance exceeds δ. If this is the case, we insert additional seeds between the respective field lines, collect these seeds for efficient parallelization, and compute them in a next pass on the GPU. We employ deletion of trajectories if they become too close to each other as an optimization to improve computation time and to save memory with the resulting curves.

4.5 Extraction of Critical Points

The critical points are obtained by repeated subdivision of those cells whose vertices exhibit opposite sign in all vector components. After subdivision, the centers of the cells that still satisfy the sign criterion at the final subdivision level represent the critical points. The procedure is carried out on the GPU in parallel. Critical points other than of type saddle, which are identified by opposite-sign real parts of the velocity gradient, are rejected. We follow the common practice to estimate the gradient at the grid nodes and to interpolate it at the critical points.

4.6 Isocline Surface Extraction and Trimming

The isocline surfaces are extracted using the Marching Cubes algorithm on the subdivided grid. In our implementation, we subdivide all cells that are initially occupied by the isosurface to the same level. Because such a direct subdivision is computationally expensive, we do not employ too many subdivision levels. After the triangle mesh from these subdivided cells has been obtained, we perform adaptive refinement of the triangle mesh. Each triangle edge between two escape vertices is tested with recursive bisection for a rest streamline, and each triangle edge between two rest vertices is tested with recursive bisection for an escape streamline. If such a sample is found, the triangle is subdivided into four subtriangles and the process is iterated a predefined number of times. In a second pass, each triangle is tested for vertices intersected by opposite type of streamlines, i.e., it is tested if one gives rise to a rest streamline and the other to an escape streamline. If this is the case, the triangle is trimmed by repeating the recursive search and final cutting.

4.7 Merging of Contours Using 1D Manifolds

As illustrated in Figs. 8(a) and 8(b), the streamsurface seeded at a seeding curve does not necessarily intersect $\partial \Omega_M$ along its full length, because there might be a saddle-type critical point leading to disruptions of the intersection curve between streamsurface and $\partial \Omega_M$. This is of no relevance to the visual result, as there will be an other streamsurface converging to the critical point from an other side and providing the missing part of the escape region boundary. These two boundary parts of the escape region converge at the spikes visible in Fig. 8(b), at the point where the 1D manifold of the critical point hits the escape
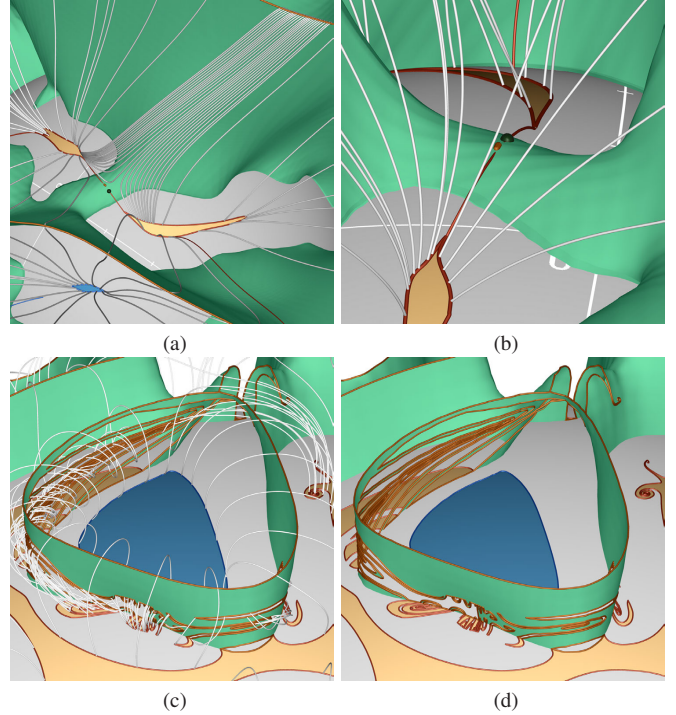

Fig. 8. Top row shows MAS data at Carrington rotation 2131. (a) Two opposite boundary curve (orange) segments give rise to streamsurface parts (one illustrated by densely seeded streamlines) that partially converge to critical point (green point) along its 1D manifold (red curve). The difficulty in this case is that the resulting intersection curves with $\partial \Omega_M$ belong to two separate escape regions (yellow). (b) Same as (a) from another view. Since the critical point is located above $\partial \Omega_M$, the intersection curves are disrupted there. The 1D manifold connects the escape regions at their tips. The bottom row shows a closeup of a complex structure in the Magma Flow that demands deep subdivision with our algorithm for extraction (twice cell and six times triangle mesh subdivision). (c) The trimmed isocline surfaces present complex boundary structures (orange), which are caused by the large vortical flow crossing $\partial \Omega_M$, as one can see by the streamlines (white) sparsely seeded at the boundary curves for context. (d) Same as (c) but without streamlines to reveal the trimmed isocline surface, as well as the escape map.

region boundary. To obtain topologically connected boundary curves also in these cases, we detect if end points of escape region boundary parts are located closer than δ to an intersection between a 1D manifold and $\partial \Omega_M$. Hence, the 1D manifolds are used to decide which end points of escape region boundaries should be merged: they are only merged if the respective seeding curves are linked via the 1D manifolds to the same critical point. But, if the escape region boundaries are only needed for display, this step can be omitted, because the end points of the curves converge extremely close to each other.

5 RESULTS

We demonstrate our technique on three examples with increasing computational complexity: (1) A buoyant flow based on a computational fluid dynamic (CFD) simulation, (2) MHD-based coronal magnetic field data, (3) a flow simulation of the magma in the Earth's mantle. Table 1 provides some timings of the shown results.

We used two levels of cell subdivision for the extraction of all isocline surfaces in our results. For the MHD data, we did not employ mesh refinement, whereas, for the Magma Flow, we further employed six iterations of adaptive mesh refinement, and three iterations for the CFD data. Increasing these levels did not change the results visually (including the patterns visible on the isoclines, which reflect the trilinear interpolation of the data). For the trimming of the boundary triangles (Sec. 4.6), we employed 50 bisection steps. However, ma-
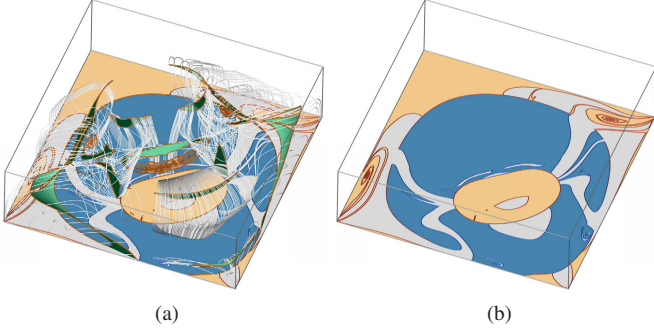
Fig. 9. Buoyant Flow CFD data. In this case $\partial\Omega_M$ is at the bottom face of Ω and the other five faces are $\partial\Omega_E$. (a) Trimmed isocline surface with seeding curves, some of the streamlines, and the resulting escape map. (b) Escape map visualizes which streamlines rise until $\partial\Omega_E$ and hence can transport heat from $\partial\Omega_M$ outside Ω.

chine precision was typically achieved with less than 50 iterations. For critical point extraction, we performed 20 subdivisions.

5.1 Buoyant Flow

The underlying dataset of the Buoyant Flow example is a CFD simulation of a closed container filled with air, which is heated at its bottom center and cooled at its top center, driving buoyant convection. The simulation grid consists of $61 \times 31 \times 61$ nodes arranged in a Cartesian grid, with extents $[0, 0.1] \times [0, 0.1] \times [0, 0.05]$. In accordance with traditional vector field topology, we take a single time step of the simulation and analyze it with our streamline-based escape map concept.

Figure 9 shows our result. Ω is set to $[0, 0.1] \times [0, 0.1] \times [0.01, 0.04]$, i.e., the map boundary is defined at $z = 0.01$ while the escape boundary reaches $z = 0.04$. Figure 9(a) shows the overall configuration of streamlines, isocline surfaces, and the resulting escape map. From the escape map in Figure 9(b) we can obtain the following insights. Our analysis reveals a system of forward (blue) and reverse (yellow) escape regions. The center of the bottom wall, where the heated plate is located, is covered by both a reverse escape region and a forward escape region, while the forward escape region is larger. This shows that hot fluid leaves the bottom boundary in a rather large area while the cold flow that comes from the top reaches the boundary in a more focused region. This example demonstrates that escape maps could be useful for the analysis of flow separation and boundary-related flow phenomena in general. Assuming that the escape boundary would lead to, e.g., open flow, the escape map could provide information where hot fluid is leaving the bottom of the chamber and hence leads to energy loss. Using a streamline probe or a set of streamlines, it would be very difficult to locate the regions at $z = 0.01$ that exhibit different streamline behavior.

5.2 Solar MHD

We use solar magnetic field data from the *Predictive Science Modeling Support for Helioseismic and Magnetic Imager Solar Dynamics Observatory* site [2] in this example. The MAS data are available with a temporal granularity of one Carrington rotation (CR), which is the period for a complete rotation of the Sun, which is about 27 days, starting from November 9, 1853. The data are given on a spherical staggered grid with resolution $181 \times 100 \times 150$ that exhibits increasing cell size in radial direction with increasing distance from the photosphere. In our implementation, we interpolate the staggered grid to a structured node-based spherical grid of the same resolution. With this conversion we avoid the implementation of special streamline integration code that operates on staggered grids, and we also ease the visualization of the field using standard techniques. The lower radial boundary of the MAS data resides slightly below the photosphere while the upper boundary is located at about $30 \cdot R_\odot$ (solar radii) and so does the grid of our converted data. Throughout our implementation, we use

trilinear interpolation consistently, both for the magnetic field (e.g., for streamline integration) and its radial component (e.g., for isocline surface extraction).

The original idea of escape maps comes from the determination of coronal holes. In this case, the map boundary $\partial\Omega_M$ is identified with the photosphere, a sphere of radius $R_\odot$, which is defined as the visible surface of the Sun. The escape boundary $\partial\Omega_E$ is set to a sphere of radius $R = 2.5R_\odot$. Then, escape regions mark the coronal holes.

In Fig. 1 the MAS data from Carrington rotation 2128 are visualized. Figure 1(a) shows the traditional approach, i.e., by view-dependent direct sampling. From this picture, it is not possible to judge which of the regions (i), (ii), (iii), and (iv) are connected. As shown in Fig. 5(a), the topology-based extraction step provides a single curve on this side of the Sun for this dataset, while Fig. 1(b) shows the trimmed isocline surfaces with some of the field lines seeded at their boundary curves, which generate the major part of the boundary curves of coronal holes, resulting in Fig. 1(c). Finally, Fig. 5(b) shows that (i), (ii), (iii), and (iv) are located within the same region of 'north' polarity but represent three distinguished coronal holes. Note that the boundaries of unipolar regions are identical to the $\partial\Omega_M$-boundary of the isocline surfaces and identical to boundary switch curves. Note also that due to this fact coronal hole boundaries cannot pass boundaries of the isocline surfaces or boundary switch curves.

The regular artifacts visible on the boundary curves of trimmed isocline surfaces (e.g., Fig. 10(c)) and on the 2D manifolds (e.g., Fig. 5(a)) are due to the trilinear interpolation scheme of the original data. The same holds for the visualization (e.g., Fig. 5(b)) which is achieved by view-dependent sampling using trilinear interpolation. These interpolation effects have no impact on the technique because the same interpolation is used in all steps, i.e., from the visualization point of view, the trilinearly interpolated field represents the true field. This consistency is also illustrated by the fact that although the seeding curve in Fig. 10(c) is not smooth, the resulting intersection curve (blue) exhibits a smooth shape.

Figure 10 shows our results for the MAS data from Carrington rotation 2131. Figure 10(a) presents a visualization similar to Fig. 1(b). There are two 'holes' in the escape regions (coronal holes), one to the left of the central isocline surface and one to the right. However, these two similar 'holes' are extracted differently. The left one is obtained by intersecting a 2D manifold of a saddle point, as shown in Fig. 10(b). This is again the only 2D manifold that contributes a boundary curve on this side of the Sun. In contrast, the right 'hole' is generated by the isocline surface-based approach, as shown in Fig. 10(c).

Figures 8(a) and (b) show Carrington rotation 2131. Figure 8(a) illustrates two issues: the divergence of a streamsurface because it hits a critical point along its 1D manifold, and the related fact that therefore a single segment on the isocline boundary seeding curve can give rise to streamsurface parts that are mapped to two distinct escape regions.

Figure 12 provides a clear picture on the morphological and topological changes of the coronal holes over four Carrington rotations, in particular regarding the appearance and disappearance of corridors. Figures 12(e)–12(h) provide a comparison with the traditional visualization technique, which fails at resolving the thin corridors.

Morphological studies of coronal hole boundaries as observed in the soft X-ray regime by the Yohkoh telescope imply that, in some unipolar regions, coronal holes may consist of several, apparently disconnected, components (see, e.g., Kahler and Hudson [12]). Antiochos' uniqueness conjecture of coronal holes, however, states that "coronal holes are unique in that every unipolar region on the photosphere can contain at most one coronal hole" [3, 27]. The apparent disconnected coronal holes were either connected by a thin, but finite, corridor, or they are linked by "singular lines of zero width".

In our experiments, we identified cases where our technique extracted more than one disconnected coronal hole in a unipolar region, one such case is shown in Fig. 5(b). We examined the influence of the choice of the escape radius R_e ($\partial\Omega_E$). Figure 11 shows a respective result for Carrington rotation 2127. One can observe changes of the coronal holes with respect to shape and topology. For example, the coronal hole located at the image center at $R_e = 1.2R_\odot$ thins down as
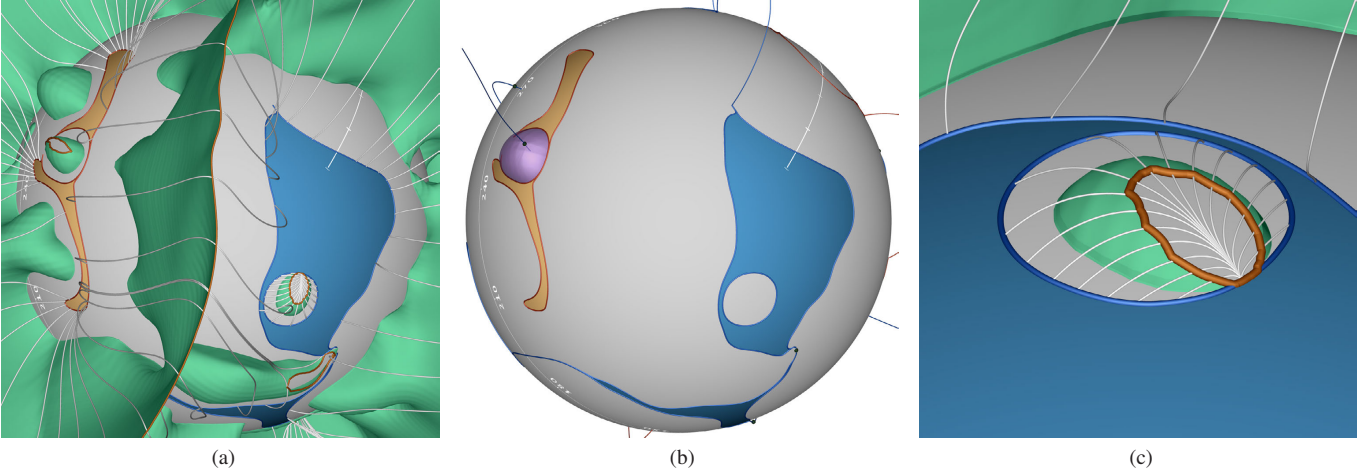
Fig. 10. MAS data at Carrington rotation 2131. (a) Trimmed isocline surface with seeding boundary curves (orange), some of the resulting field lines (white), and the resulting coronal hole boundaries (red, blue). (b) Only a single boundary curve segment is contributed by the topology-based approach (2D manifold in transparent pink together with 1D manifolds). Note that the 2D manifold does neither reach $\partial\Omega_M$ everywhere, nor does it reach $\partial\Omega_E$ (Fig. 4(c)), instead it contributes a geometrically open segment. (c) Closeup of 'hole' in blue region. This represents the rather rare case of Fig. 4(d) (ii) covered by Step 4. in Sec. 3.2.2. The 'purple' segment (boundary switch curve) is the part of the orange boundary curve at $\partial\Omega_M$.
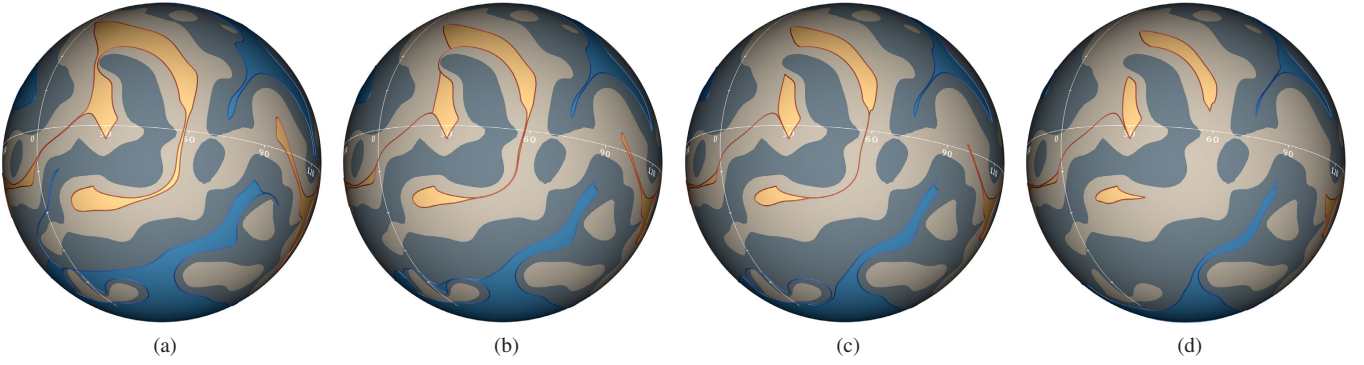

Fig. 11. MAS data at Carrington rotation 2127. Coronal hole boundaries and polarity of the photosphere (blueish 'north', yellowish 'south') for escape radii $R_e = 1.2R_\odot$ (a), $R_e = 1.35R_\odot$ (b), $R_e = 1.5R_\odot$ (c), and $R_e = 2.5R_\odot$ (d). More disconnected coronal holes per unipolar region are obtained with large R_e and that also the genus of the coronal holes can change (the closed corridor at the bottom disappears between (c) and (d)).

R_e increases and represents a corridor there at $R_e = 1.5R_\odot$, before it vanishes for $R_e = 2.5R_\odot$. Using $R_e > 2.5R_\odot$ did not result in further substantial changes of the coronal holes. This contradicts Antiochos' conjecture. However, detailed investigations have to be subject of future research in the field of astrophysics and scientific visualization.

5.3 Magma Flow

The Magma Flow dataset was obtained using CitcomS [1], which is a finite element code designed to solve compressible thermochemical convection problems relevant to Earth's mantle. In contrast to the MHD dataset, the magma flow presents more complex structures like large vortical flows convecting magma between deep and surface-proximate Earth mantle regions. The analysis of the dynamics of this flow and a mapping of mass transport between the different levels of depth inside the Earth can support the understanding of volcanic processes and the movement of plate tectonics, which can also facilitate studies about prediction of volcanic eruption or earthquakes. Here, we used a global simulation domain given on a spherical grid of resolution $315 \times 157 \times 24$. Aiming to capture special cases of high complexities for our algorithm, and to avoid the high computation time of extracting subdivided isocline surfaces for such a large and complex dataset, we setup the map and escape boundaries as two spheres of radii $R_M = 0.8R_\oplus$ (earth radii) and $R_E = 0.9R_\oplus$. In this configuration, we could capture some cases of vortices intersecting $\partial\Omega_M$, for

example, the case shown in Figs. 8(c), 8(d), and 13. To this dataset, we have applied cell subdivision and adaptive mesh subdivision with depths two and six, respectively. For integration, we performed a maximum of three thousand steps of size 0.0005. Note that this dataset has higher resolution than the Buoyant Flow dataset and it also needs even deeper mesh subdivision. Both yields in a computation time of about two and a half hours for the extraction of its trimmed isocline surfaces.

Table 1. Performance measurements. Initial mesh and cell subdivision (init.), adaptive mesh refinement (adapt.), mesh boundary refinement (bound.), boundary advection (advec.), and total extraction time (total).

| Data Source	Time [s]				
	init.	adapt.	bound.	advec.	total
Magma Flow	52.69	2930.55	5336.94	48.04	8371.46
Solar CR2131	515.84	0.52	193.05	410.80	1121.33
Solar CR2125	596.38	0.57	180.64	172.33	951.05
Solar CR2126	521.97	0.53	156.14	1264.22	1943.95
Solar CR2127	516.08	0.55	141.19	388.80	1047.73
Solar CR2128	585.21	0.61	179.77	410.81	1177.64
Buoyant Flow	30.67	309.01	965.78	10.75	1316.68
Analytic ($\lambda = 2$)	2.64	6.91	24.24	2.15	36.00
Analytic ($\lambda = 10$)	3.38	8.63	16.80	1.82	30.68
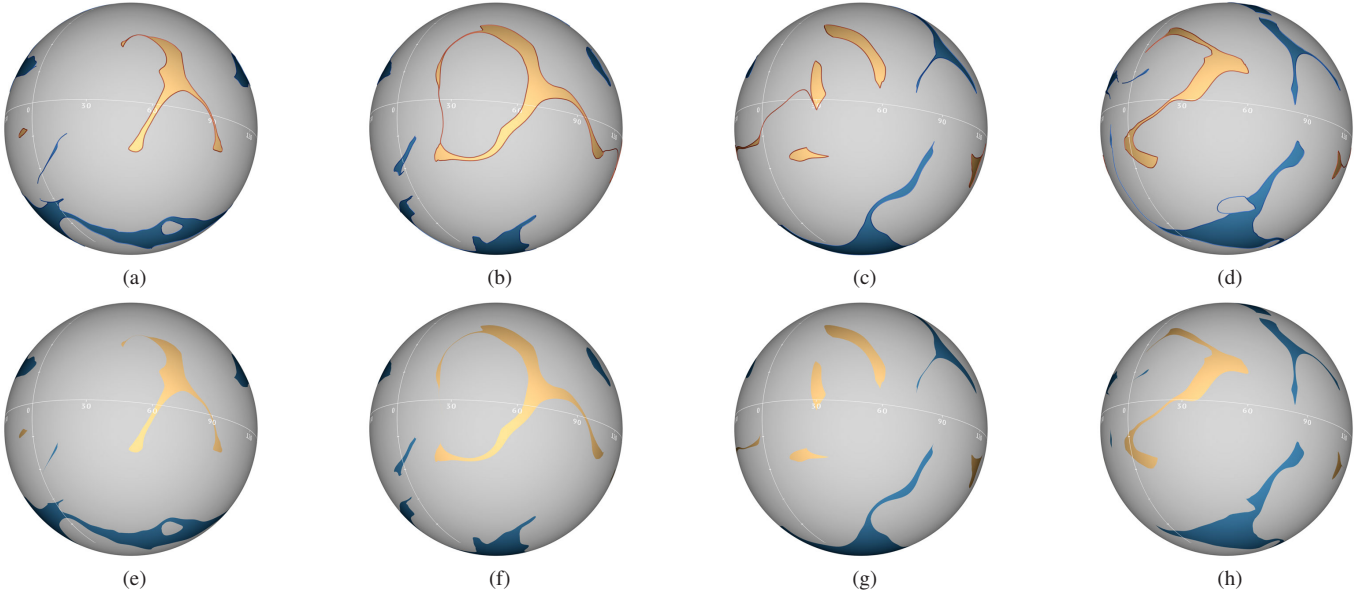
Fig. 12. MAS data for Carrington rotations 2125 (a), 2126 (b), 2127 (c), and 2128 (d). Due to the clear representation of the corridors by our technique, one can easily observe topological changes of the coronal holes. See Fig. 11 for the polarity of the photosphere in case of (c). (e)–(h): Same as (a)–(d) but with traditional direct sampling approach. It is apparent that, again, this approach is not able to resolve the corridors.
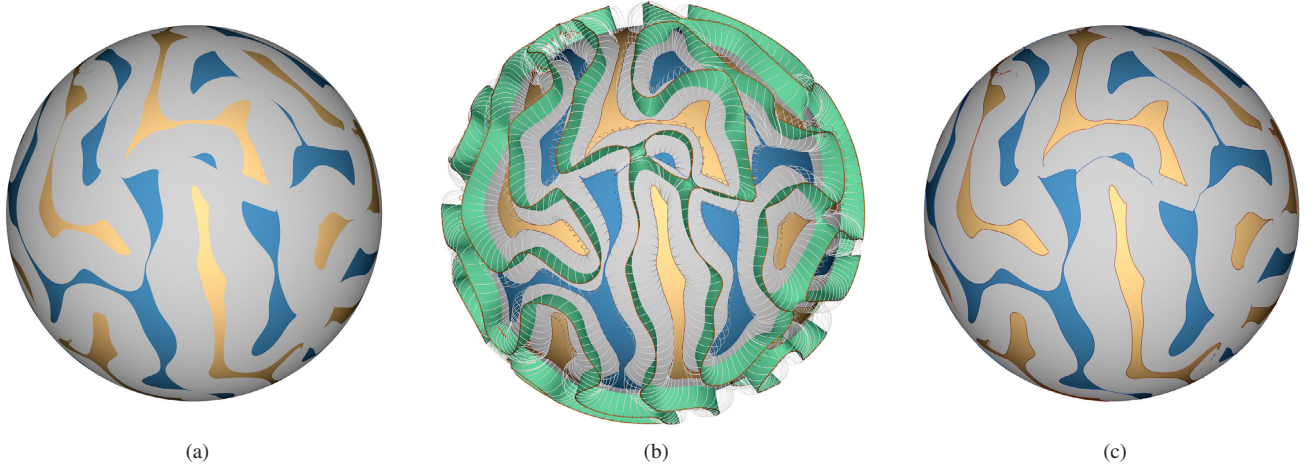

Fig. 13. Escape maps of Magma Flow dataset. $\partial\Omega_M$ and $\partial\Omega_E$ are positioned at radii $R_M = 0.8R_\oplus$ and $R_E = 0.9R_\oplus$, respectively. The map indicates regions at $R_M = 0.8R_\oplus$ from where the flow reaches $R_E = 0.9R_\oplus$ in forward (blue) and backward (yellow) direction. (a) Visualization with the view-dependent direct sampling approach. This approach suffers from sampling issues and cannot capture the full topological structure of the escape regions. Note that it is not possible to judge the connections between the apparent escape regions. (b) Our approach, see Figs. 8(c) and (d) for a closeup. (c) Resulting escape map, according to our approach, provides full topological structure.

6   CONCLUSION

We have presented a technique for topologically correct and robust extraction of escape maps, which show if a streamline emanating from a given position on the map in forward or reverse direction leaves an adjacent, arbitrarily-shaped simply-connected region. The concept of escape maps was inspired from astrophysics, where it is equivalent to the problem of extracting coronal holes on the Sun's photosphere. In contrast to the traditional approach that discretizes the map and therefore suffers from discretization issues, our approach builds on isocline surfaces of the vector field to obtain a seeding tailored at the topologically correct extraction of escape maps. Our approach provides several benefits. First and most important, it is able to extract very narrow map structures, in contrast to the traditional approach that suffers severely from aliasing. This becomes particularly obvious in case of the extraction of coronal hole corridors, which are missed by traditional approaches and are subject to current research in astrophysics.

Second, it performs field line integration in these cases in the more stable direction toward the map boundary, avoiding prohibitive accumulation of integration error.

The concept of escape maps is closely related to vector field topology on bounded domains. Nevertheless, in our understanding, further research is necessary to clearly determine possible links and properties between these two concepts, and if escape maps could provide a basis for such a vector field topology. Finally, we hope to inspire future research on the connection between isocline surfaces and topological features, and to call attention to isocline surfaces for scientific visualization in general.

REFERENCES

[1] CitcomS. http://geodynamics.org/cig/software/citcoms.

[2] Predictive Science Modeling Support for Helioseismic and Magnetic Imager Solar Dynamics Observatory.
http://www.predsci.com/hmi/home.php.

[3] S. K. Antiochos, C. R. DeVore, J. T. Karpen, and Z. Mikić. Structure and dynamics of the Sun's open magnetic field. *The Astrophysical Journal*, 671(1):936–946, 2007.

[4] D. Asimov. Notes on the topology of vector fields and flows. Technical Report RNR-93-003, NASA Ames Research Center, 1993.

[5] S. Bachthaler, F. Sadlo, R. Weeber, S. Kantorovich, C. Holm, and D. Weiskopf. Magnetic flux topology of 2D point dipoles. *Computer Graphics Forum*, 31(3):955–964, 2012.

[6] D. Cai, B. Lembege, and K. Nishikawa. Visualizing magnetospheric vector field topology. In *Proceedings of ISSS-7*, pages 26–31, 2005.

[7] S. R. Cranmer. Coronal holes. *Living Reviews in Solar Physics*, 6(3), 2009.

[8] A. Globus, C. Levit, and T. Lasinski. A tool for visualizing the topology of three-dimensional vector fields. In *Proceedings of IEEE Visualization*, pages 33–40, 408, 1991.

[9] J. L. Helman and L. Hesselink. Representation and display of vector field topology in fluid flow data sets. *Computer*, 22(8):27–36, 1989.

[10] J. L. Helman and L. Hesselink. Visualizing vector field topology in fluid flows. *IEEE Computer Graphics and Applications*, 11(3):36–46, 1991.

[11] J. P. M. Hultquist. Constructing stream surfaces in steady 3D vector fields. In *Proceedings of IEEE Visualization*, pages 171–178, 1992.

[12] S. W. Kahler and H. S. Hudson. Boundary structures and changes in long-lived coronal holes. *The Astrophysical Journal*, 574(1):467–476, 2002.

[13] J. Kasten, J. Reininghaus, W. Reich, and G. Scheuermann. Toward the extraction of saddle periodic orbits. In *Topological Methods in Data Analysis and Visualization III*, Mathematics and Visualization, pages 55–69. Springer International Publishing, 2014.

[14] L. Krista and P. Gallagher. Automated coronal hole detection using local intensity thresholding techniques. *Solar Physics*, 256:87–100, 2009.

[15] G. M. Machado, F. Sadlo, and T. Ertl. Local extraction of bifurcation lines. In *Proceedings of International Workshop on Vision, Modeling and Visualization*, pages 17–24, 2013.

[16] G. M. Machado, F. Sadlo, and T. Ertl. Image-based streamsurfaces. In *Proceedings of 27th SIBGRAPI Conference on Graphics, Patterns and Images*, 2014. to appear.

[17] G. M. Machado, F. Sadlo, T. Müller, D. Müller, and T. Ertl. Visualizing solar dynamics data. In *Proceedings of International Workshop on Vision, Modeling and Visualization*, pages 95–102, 2012.

[18] D. Mackay and A. Yeates. The Sun's global photospheric and coronal magnetic fields: Observations and models. *Living Reviews in Solar Physics*, 9(6), 2012.

[19] M. Otto, T. Germer, and H. Theisel. Uncertain topology of 3D vector fields. In *Proceedings of 4th IEEE Pacific Visualization Symposium*, pages 67–74, China, 2011.

[20] M. Otto and H. Theisel. Vortex analysis in uncertain vector fields. *Computer Graphics Forum*, 31(3pt2):1035–1044, 2012.

[21] R. Peikert and F. Sadlo. Topology-guided visualization of constrained vector fields. In *Topology-Based Methods in Visualization*, pages 21–34. Springer-Verlag, 2007.

[22] A. E. Perry and M. S. Chong. A description of eddying motions and flow patterns using critical-point concepts. *Annual Review of Fluid Mechanics*, 19:125–155, 1987.

[23] P. Riley, J. A. Linker, Z. Miki, R. Lionello, S. A. Ledvina, and J. G. Luhmann. A comparison between global solar magnetohydrodynamic and potential field source surface model results. *The Astrophysical Journal*, 653(2):1510–1516, 2006.

[24] G. Scheuermann, B. Hamann, K. I. Joy, and W. Kollmann. Visualizing local vector field topology. *SPIE Journal of Electronic Imaging*, 9:356–367, 2000.

[25] H. Theisel, T. Weinkauf, H.-C. Hege, and H.-P. Seidel. Saddle connectors – An approach to visualizing the topological skeleton of complex 3D vector fields. In *Proceedings of IEEE Visualization*, pages 225–232, 2003.

[26] J. F. Thompson, B. K. Soni, and N. P. Weatherill. *Handbook of Grid Generation*. Taylor & Francis, 1998.

[27] V. S. Titov, Z. Mikić, J. A. Linker, R. Lionello, and S. K. Antiochos. Magnetic topology of coronal hole linkages. *The Astrophysical Journal*, 731(2):111, 2011.

[28] M. Üffinger, F. Sadlo, and T. Ertl. A time-dependent vector field topology based on streak surfaces. *IEEE Transactions on Visualization and Computer Graphics*, 19(3):379–392, 2013.

[29] T. Weinkauf, H. Theisel, H.-C. Hege, and H.-P. Seidel. Boundary switch connectors for topological visualization of complex 3D vector fields. In *Proceedings of the Symposium on Visualization*, pages 183–192, 2004.

[30] T. Wischgoll and G. Scheuermann. Locating closed streamlines in 3D vector fields. In *Proceedings of the Symposium on Data Visualisation*, pages 227–232, 2002.